Geophysical Journal International

Geophys. J. Int. (2017) **208,** 1724–1739
Advance Access publication 2016 December 22
GJI Rock and mineral physics, rheology

doi: 10.1093/gji/ggw476

Anisotropic attenuation in rocks: theory, modelling and lab measurements

Václav Vavryčuk,[1] Tomáš Svitek[2] and Tomáš Lokajíček[2]

[1] *Institute of Geophysics, The Czech Academy of Sciences, Boční* II/1401, 14100 *Praha, Czech Republic. E-mail: vv@ig.cas.cz*
[2] *Institute of Geology, The Czech Academy of Sciences, Rozvojová* 269, 16500 *Praha, Czech Republic*

Accepted 2016 December 20. Received 2016 December 17; in original form 2016 May 21

SUMMARY

Anisotropic attenuation affects seismic observations and complicates their interpretations. Its accurate determination is, however, difficult and needs extensive measurements of wavefields in many directions. So far, the traveltime and amplitude decay of waves are usually measured along a sparse grid of propagation directions, and methods for inverting for anisotropic attenuation are not fully developed. In this paper, we present theory allowing a description and parametrization of general triclinic anisotropic attenuation. We focus on a correct recalculation of ray quantities usually measured in lab to phase quantities needed in the inversion. We develop and numerically test an iterative inversion scheme for determining the parameters of anisotropic attenuation. We present a lab facility that allows for measuring anisotropic attenuation using the *P*-wave ultrasonic sounding of spherical samples in 132 directions distributed regularly over the sphere. The applicability of the proposed inversion method and the performance of the experimental setup are exemplified by determining triclinic anisotropic attenuation of the serpentinite rock from Val Malenco, Northern Italy. The ray velocity and ray attenuation were measured on a spherical sample of the rock with diameter of 45.5 mm at the room temperature and under two pressure levels: 0.1 and 20 MPa. The measurements confirmed that anisotropic attenuation is remarkably sensitive to confining pressure. Since cracks are closing with increasing pressure, attenuation decreases. However, changes in pressure can also induce changes in the directional variation of attenuation and rotation of anisotropy axes. The obtained results for the serpentinite rock sample are unique because they represent the first accurately determined triclinic anisotropic attenuation from lab measurements.

Key words: Elasticity and anelasticity; Body waves; Seismic anisotropy; Seismic attenuation.

1 INTRODUCTION

Many rocks of the lithosphere and uppermost mantle are seismically anisotropic and attenuating (Babuška & Cara 1991; Savage 1999; Romanowicz 2003; Fouch & Rondenay 2006). These two phenomena are closely related and jointly affect the seismic waves (Burton 2007; Carcione 2014). They cause that the propagation velocity of seismic waves and dissipation of energy are directionally dependent and the signal is dispersive. Anisotropy and dispersion complicates modelling of wave propagation as well as interpretation of seismic observations.

Anisotropic velocity and attenuation are efficiently described using a model of viscoelastic anisotropy. The viscoelastic parameters are complex-valued and frequency dependent (Auld 1973; Carcione 2014). Their real and imaginary parts describe elastic and attenuation anisotropy, respectively. The use of complex algebra allows for generalizing the theory developed for elastic anisotropy to viscoelastic anisotropy. The equations for waves in viscoelastic media are formally the same as in elastic media except for being complex. Implementing complex algebra into equations is mathematically straightforward, but still some care is needed for understanding properly the physical meaning of all complex-valued quantities in the equations.

The model of viscoelastic anisotropy has been successfully applied in theoretical studies of propagation of plane waves (Shuvalov & Scott 1999; Červený & Pšenčík 2005; Zhu & Tsvankin 2006; Borcherdt 2009; Rasolofosaon 2010) as well as of waves radiated by point sources (Carcione 1990, 1993, 1994; Gajewski & Pšenčík 1992; Carcione *et al.* 1996; Vavryčuk 2007b). The exact and asymptotic Green's functions for homogeneous media were derived (Vavryčuk 2007a), complex and real ray-tracing techniques in smoothly inhomogeneous media and in media with interfaces were developed (Hearn & Krebes 1990; Hanyga & Seredynska 2000; Vavryčuk 2008a, 2010). It was recognized that similarly to differentiating between the phase and ray velocities in elastic media, the phase and ray attenuation must be distinguished in attenuating media (Vavryčuk 2007b, 2015).

Anisotropic attenuation of rocks and other materials has been modelled theoretically (Mukerji & Mavko 1994; Carcione 2000; Chapman 2003; Wenzlau *et al*. 2010) and also measured in laboratory (Johnston & Toksöz 1980; Kim *et al*. 1983; Kern *et al*. 1997; Stanchits *et al*. 2003; Zhu *et al*. 2007). So far, most experiments were based on measuring elastic properties and attenuation of rocks by ultrasonic waves propagating in a limited range of directions of cubic, block or cylindrical rock samples (Hosten *et al*. 1987; Kern *et al*. 1997; Stanchits *et al*. 2003). Therefore, they allowed for rough estimating anisotropic attenuation of high symmetry only. The elastic anisotropy has also been measured on spherical rock samples (Pros *et al*. 1998, 2003; Lokajíček *et al*. 2014; Svitek *et al*. 2014). Such arrangement is more convenient and robust because it allows for measuring rock properties in a rather high number of uniformly distributed directions, which is necessary for determining parameters of general anisotropy. On the other hand, the inversion of measurements on spherical samples is more involved. The standard schemes are based on the inversion of phase quantities, which are related to propagation of plane waves. However, in lab experiments on spherical samples, waves with curved wave fronts are generated and the ray quantities are measured and interpreted. Similarly, field experiments provide usually measurements of ray rather than phase quantities.

In this paper, we extend the approach originally developed for studying general elastic anisotropy on spherical samples by incorporating measurements of anisotropic attenuation. We extend the theory of inversion for viscoelastic anisotropy presented by Vavryčuk (2015) to be applicable to measurements in lab or field experiments. Specifically, we focus on the following unsolved issues: (1) how to calculate ray attenuation from amplitudes of signals propagated in anisotropic rocks, (2) how to eliminate effects of elastic anisotropy in amplitudes of waves and (3) how to construct the complex phase velocity surface from the complex energy velocity surface, which is a necessary step before applying an inversion scheme for parameters of viscoelastic triclinic anisotropy. The accuracy and robustness of the developed approach is numerically tested. It is shown that the inversion is applicable to weak as well as strong anisotropy. Finally, we demonstrate the determination of parameters of anisotropic attenuation on measurements of the serpentinite rock from Val Malenco, Northern Italy studied by Kern *et al*. (1997).

2 ANISOTROPIC VISCOELASTIC MEDIA

In this section, basic formulae for waves propagating in anisotropic viscoelastic media are shortly reviewed. In the formulae, real and imaginary parts of complex-valued quantities are denoted by superscripts R and I. The complex-conjugate quantity is denoted by an asterisk. The magnitude of complex-valued vector $\mathbf{v}$ is $\sqrt{\mathbf{v}\cdot\mathbf{v}}$. If any complex-valued vector has a real-valued direction, it is called homogeneous. If its direction is complex, it is called inhomogeneous. In formulae, the Einstein summation convention is used for repeated subscripts.

2.1 Viscloelastic parameters

A viscoelastic anisotropic medium is defined by density-normalized stiffness parameters $a_{ijkl} = c_{ijkl}/\rho$ which are, in general, frequency-dependent and complex-valued. The real and imaginary parts of a_{ijkl},

$$a_{ijkl}(\omega) = a^R_{ijkl} + i\, a^I_{ijkl}, \tag{1}$$

define elastic and viscous properties of the medium. The Christoffel tensor Γ_{jk}

$$\Gamma_{jk}(\mathbf{p}) = a_{ijkl}\, p_i\, p_l, \tag{2}$$

is frequency-dependent and complex. Similarly as in elastic media, the eigenvalue of the Christoffel tensor and its derivative are expressed (Červený 2001)

$$G(\mathbf{p}) = a_{ijkl}\, p_i\, p_l\, g_j\, g_k = 1, \tag{3}$$

$$v_i = \frac{1}{2}\frac{\partial G(\mathbf{p})}{\partial p_i} = a_{ijkl}\, p_l\, g_j\, g_k, \tag{4}$$

where $\mathbf{p}$ is the slowness vector $\mathbf{p} = \mathbf{n}/c$, c is the complex phase velocity, $\mathbf{n}$ is the complex slowness direction and $\mathbf{v}$ is the complex energy velocity vector. The polarization vector $\mathbf{g}$ is calculated as the eigenvector of the Christoffel tensor and normalized as $\mathbf{g}\cdot\mathbf{g} = 1$. A more common normalization in complex algebra $\mathbf{g}\cdot\mathbf{g}^* = 1$ is not used because it leads to inconsistencies between equations in elastic and viscoelastic media. Vectors $\mathbf{v}$ and $\mathbf{p}$ are related by the equation,

$$\mathbf{v}\cdot\mathbf{p} = 1, \tag{5}$$

expressing their polar reciprocity similarly as in elastic media (Helbig 1994).

The above equations are formally the same for elastic and viscoelastic media. They just differ in whether the wave quantities are real or complex. The wave quantities are real in elastic media but generally complex in viscoelastic media.

2.2 Phase and ray quantities

The phase quantities describe propagation of plane waves and are obtained by decomposing the complex slowness vector $\mathbf{p}$:

$$\mathbf{p} = \left[\left(V^{\text{phase}}\right)^{-1} + i\, A^{\text{phase}}\right]\mathbf{n}^{||} + i\, D^{\text{phase}}\,\mathbf{n}^{\perp}, \tag{6}$$

where V^{phase}, A^{phase} and D^{phase} are the real phase velocity, phase attenuation and phase inhomogeneity. Vectors $\mathbf{n}^{||}$ and $\mathbf{n}^{\perp}$ are real, mutually perpendicular unit vectors, $\mathbf{n}^{||}$ is normal to the wave front and $\mathbf{n}^{\perp}$ lies in the wave front. The phase inhomogeneity D^{phase} depends on the boundary conditions. If D^{phase} is known, the phase velocity V^{phase} and attenuation A^{phase} are uniquely determined from the eikonal equation (3). If D^{phase} is zero, slowness vector $\mathbf{p}$ is homogeneous, its direction $\mathbf{n}$ is real and coincides with $\mathbf{n}^{||}$. Velocity V^{phase} and attenuation A^{phase} are then called intrinsic.

The ray quantities describe propagation of energy along a ray. They are obtained by decomposing the complex energy velocity vector $\mathbf{v}$:

$$\mathbf{v} = \left[\left(V^{\text{ray}}\right)^{-1} + i\, A^{\text{ray}}\right]^{-1}\mathbf{N}^{||} + i\, D^{\text{ray}}\,\mathbf{N}^{\perp}, \tag{7}$$

where V^{ray}, A^{ray} and D^{ray} are the real ray velocity, ray attenuation and ray inhomogeneity. Vectors $\mathbf{N}^{||}$ and $\mathbf{N}^{\perp}$ are real, mutually perpendicular unit vectors. The ray inhomogeneity D^{ray} depends on the boundary conditions. For point sources situated in homogeneous media, D^{ray} is zero (see Vavryčuk 2007a). In this case, energy velocity vector $\mathbf{v}$ is homogeneous, its direction $\mathbf{N}$ is real and coincides with $\mathbf{N}^{||}$ (see appendix F of Carcione & Ursin 2016). Velocity V^{ray}

and attenuation A^{ray} are then called intrinsic, similarly as for the phase quantities.

The intrinsic phase and ray quantities are related to the complex phase velocity c and complex energy velocity v as follows:

$$\frac{1}{c} = \frac{1}{V^{\mathrm{phase}}} + i\,A^{\mathrm{phase}}, \quad \frac{1}{v} = \frac{1}{V^{\mathrm{ray}}} + i\,A^{\mathrm{ray}}, \tag{8}$$

hence

$$V^{\mathrm{phase}} = \frac{c^R c^R + c^I c^I}{c^R}, \quad V^{\mathrm{ray}} = \frac{v^R v^R + v^I v^I}{v^R}, \tag{9}$$

$$A^{\mathrm{phase}} = -\frac{c^I}{c^R c^R + c^I c^I}, \quad A^{\mathrm{ray}} = -\frac{v^I}{v^R v^R + v^I v^I}, \tag{10}$$

$$Q^{\mathrm{phase}} = -\frac{\left(c^2\right)^R}{\left(c^2\right)^I}, \quad Q^{\mathrm{ray}} = -\frac{\left(v^2\right)^R}{\left(v^2\right)^I}, \tag{11}$$

where

$$v = \sqrt{v_i v_i} \text{ and } c = 1/\sqrt{p_i p_i}. \tag{12}$$

The intrinsic complex phase velocity c is calculated straightforwardly using the eikonal equation (3), but calculating the intrinsic complex energy velocity v using eq. (4) is more involved. It requires computing the so-called 'stationary' slowness vector $\mathbf{p}_0$ introduced in ray theory (Vavryčuk 2007a). The stationary slowness vector is generally inhomogeneous being uniquely constrained by the boundary conditions. It can be calculated by complex ray tracing (Kravtsov *et al.* 1999; Hanyga & Seredynska 2000; Vavryčuk 2008a, 2010, 2012) and corresponds to a ray connecting the source of waves with a receiver. While the source and receiver are points in real space, the ray is a curve in complex space. The problem is simplified in homogeneous media, where the ray becomes a straight line in real space. To determine the stationary slowness vector in homogeneous media, either a system of polynomial equations for unknown components of $\mathbf{p}_0$ or an inverse problem for $\mathbf{p}_0$ must be solved for each ray coming out of the source (for details, see Vavryčuk 2007a,b).

2.3 Asymptotic Green's function

Radiation of waves generated by a point source is usually calculated using the Green's function. The asymptotic Green's function in homogeneous anisotropic viscoelastic media reads (Vavryčuk 2007a, his eq. 18):

$$G_{kl}\left(\mathbf{x}, \omega\right) = \frac{1}{4\pi\rho}\,\frac{g_k g_l}{v\sqrt{|K|}}\,\frac{1}{r}\,\exp\left(i\sigma_0 + i\omega\,\mathbf{p}_0\cdot\mathbf{x}\right), \tag{13}$$

or

$$G_{kl}\left(\mathbf{x}, \omega\right) = \frac{1}{4\pi\rho}\,\frac{g_k g_l}{v\sqrt{|K|}}\,\frac{1}{r}\,\exp\left(i\sigma_0\right)\,\exp\left(-\omega\,A^{\mathrm{ray}} r\right) \times \exp\left(i\omega\,\frac{r}{V^{\mathrm{ray}}}\right), \tag{14}$$

where

$$\sigma_0 = -\frac{1}{2}\left(\varphi_1 + \varphi_2\right), \quad -\frac{3}{2}\pi \le \varphi_1 < \frac{1}{2}\pi, \quad -\frac{3}{2}\pi \le \varphi_2 < \frac{1}{2}\pi,$$

and $\mathbf{p}_0$ is the stationary slowness vector (see Vavryčuk 2007a,b). Quantity $K = K_1 K_2$ is the Gaussian curvature of the slowness surface, K_1 and K_2 are the principal curvatures and φ_1 and φ_2 are their phase angles. All quantities dependent on $\mathbf{p}$ in eqs (13) and (14) are taken at stationary point $\mathbf{p}_0$. Position vector $\mathbf{x} = r\mathbf{N}$, distance r, ray vector $\mathbf{N}$, frequency ω, phase angles φ_1 and φ_2 and density ρ are real-valued; but polarization vector $\mathbf{g}$, Gaussian curvature K, principal curvatures K_1 and K_2, energy velocity v and slowness vector $\mathbf{p}_0$ are complex-valued. The most efficient way how to calculate the Gaussian curvature K in eqs (13) and (14) is by computing the determinant of the wave metric tensor (see Vavryčuk 2003, his eqs 10 and 15).

3 INVERSION FOR VISCOELASTIC ANISOTROPY

3.1 Phase and ray measurements

The parameters of anisotropic attenuating media can be determined from a directionally dependent phase or ray velocity and attenuation. The phase quantities are measured if the source of waves has a finite dimension and can generate a planar wave front. If the source is much smaller than the distance between the source and the receiver (the so-called point-like source), the wave front is curved and the ray quantities are measured. Since inverting phase quantities is computationally much simpler than inverting ray quantities, measurements of the phase velocity and attenuations are preferable. From the phase quantities, we can directly construct the complex phase velocity and then invert it for parameters of viscoelastic anisotropy.

However, devising an experiment with planar wave fronts excited and propagating in a medium in many directions is complicated. Instead, we often measure just ray quantities on wave fronts generated by a point-like source. In this case, the problem is more involved and we have to first recalculate the ray quantities to the phase quantities before inverting them for parameters of viscoelastic anisotropy.

3.2 Ray velocity and attenuation

In lab or field experiments, propagation time of a signal along a ray and its amplitude are usually measured. Determining ray velocity from propagation time is straightforward but determining ray attenuation from amplitudes of the signal is more involved. The attenuation must be calculated from amplitude decay of a signal obtained as the difference between amplitudes measured at two points of a ray and corrected for geometrical spreading.

If the amplitude decay is measured along the source–receiver distance, the amplitudes must be corrected for the radiation pattern of a source (see eq. 13)

$$C_{kl} = \frac{1}{4\pi\rho}\,\frac{g_k g_l}{v\sqrt{|K|}}. \tag{15}$$

Assuming the emitter and receiver of waves oriented along ray direction $\mathbf{N}$, the radiation function takes the following form:

$$R = \frac{1}{4\pi\rho}\,\frac{g_k g_l N_k N_l}{v\sqrt{|K|}}. \tag{16}$$

The radiation function R in eq. (16) is complex and directionally dependent in anisotropic viscoelastic media. The imaginary part of R introduces phase shifts of the signal but the amplitude of the signal is influenced negligibly. If we focus on processing of amplitudes only, the radiation function R for attenuation anisotropy can be well approximated by that in elastic anisotropy. In this way, we can separate the effects of elastic anisotropy and attenuation and determine ray attenuation in the following way:

(1) We determine elastic anisotropy of a rock from measurements of the ray velocity (Svitek *et al.* 2014).

(2) We calculate the radiation pattern and geometrical spreading of elastic waves propagating in the anisotropic rock.

(3) We correct the measured amplitude decay of the signal for these two factors and normalize the corrected value to a unit ray length.

3.3 Complex phase velocity

Having calculated ray velocity V^{ray} and ray attenuation A^{ray}, we determine the complex energy velocity v for a set of ray directions $\mathbf{N}$ using eq. (8) and construct the complex energy velocity surface $v = v(\mathbf{N})$. Decomposing the energy velocity vector $\mathbf{v}$ and the slowness vector $\mathbf{p}$ into their real and imaginary parts, the polar reciprocity relation (5) reads

$$\mathbf{v}^R \cdot \mathbf{p}^R - \mathbf{v}^I \cdot \mathbf{p}^I = 1, \tag{17}$$

$$\mathbf{v}^R \cdot \mathbf{p}^I + \mathbf{v}^I \cdot \mathbf{p}^R = 0. \tag{18}$$

Taking into account that vector $\mathbf{v}$ is homogeneous

$$\mathbf{v}^R = v^R \mathbf{N}, \quad \mathbf{v}^I = v^I \mathbf{N}, \tag{19}$$

and vector $\mathbf{p}$ is inhomogeneous

$$\mathbf{p}^R = p^R \mathbf{s}^R, \quad \mathbf{p}^I = p^I \mathbf{s}^I, \tag{20}$$

where $\mathbf{N}$ is the real ray direction, and $\mathbf{s}^R$ and $\mathbf{s}^I$ are real directions of vectors $\mathbf{p}^R$ and $\mathbf{p}^I$, respectively, eqs (17) and (18) imply

$$p^I = -\frac{v^I}{v^R} \frac{\mathbf{N} \cdot \mathbf{s}^R}{\mathbf{N} \cdot \mathbf{s}^I} p^R, \tag{21}$$

and consequently

$$p^R = \frac{v^R}{v^R v^R + v^I v^I} \quad \frac{1}{\mathbf{N} \cdot \mathbf{s}^R}, \tag{22}$$

$$p^I = -\frac{v^I}{v^R v^R + v^I v^I} \quad \frac{1}{\mathbf{N} \cdot \mathbf{s}^I}. \tag{23}$$

Finally, complex slowness vector $\mathbf{p}$ is

$$\mathbf{p} = p^R \mathbf{s}^R + i\, p^I \mathbf{s}^I, \tag{24}$$

and its direction

$$\mathbf{n} = \frac{\mathbf{p}}{\sqrt{\mathbf{p} \cdot \mathbf{p}}}. \tag{25}$$

The above equations can be used for calculating the complex slowness surface $p = p(\mathbf{n})$ from the complex energy velocity surface $v = v(\mathbf{N})$. First, we calculate real unit vectors $\mathbf{s}^R$ and $\mathbf{s}^I$ as the normals to the real part $v^R = v^R(\mathbf{N})$ and the imaginary part $v^I = v^I(\mathbf{N})$ of the energy velocity surface $v = v(\mathbf{N})$. Since surfaces $v^R = v^R(\mathbf{N})$ and $v^I = v^I(\mathbf{N})$ are real, we can use standard formulae of differential geometry (Lipschutz 1969). Then, we calculate p^R and p^I using eqs (22) and (23), and subsequently the complex slowness vectors $\mathbf{p}$ and its direction $\mathbf{n}$ using eqs (24) and (25).

If the procedure is applied to a sufficiently dense set of ray directions $\mathbf{N}$, we can construct the whole slowness surface $p = p(\mathbf{n})$ and subsequently the complex phase velocity surface $c = c(\mathbf{n})$:

$$c = v\, \mathbf{N} \cdot \mathbf{n}, \tag{26}$$

and invert for parameters of viscoelastic anisotropy.

3.4 Inversion scheme

Determination of complex viscoelastic parameters a_{ijkl} from the complex phase velocity surface $c = c(\mathbf{n})$ is a non-linear inverse problem which can be solved using perturbation theory and iterations (Mensch & Rasolofosaon 1997; Vavryčuk 2008b, 2015; Svitek *et al.* 2014). In perturbation theory, we assume that the anisotropic medium defined by unknown parameters a_{ijkl} can be obtained by a small perturbation of a known reference medium

$$a_{ijkl} = a^0_{ijkl} + \Delta a_{ijkl}, \tag{27}$$

where a^0_{ijkl} defines the viscoelastic reference medium and Δa_{ijkl} its viscoelastic perturbation. Under this assumption, the cubic equation for the square of the phase velocity c^2 can be linearized as follows (Pšenčík & Vavryčuk 2002; Svitek *et al.* 2014):

$$\Delta c^2 = c^2 - c_0^2 = \Delta a_{ijkl} n_i n_l g^0_j g^0_k, \tag{28}$$

where c_0 and $\mathbf{g}^0$ define the complex phase velocity and complex polarization vector in the reference medium, Δc^2 is the misfit between the squared phase velocity calculated from measurements and the velocity in the reference medium. The reference medium can be isotropic or anisotropic, elastic or viscoelastic. From perturbations Δa_{ijkl}, we obtain parameters a_{ijkl} using eq. (28). This new medium serves as the reference medium in the next iteration. The iterations are repeated until perturbations Δa_{ijkl} are negligibly small. The number of iterations depends on anisotropy strength: the stronger the viscoelastic anisotropy is, the more iterations are needed. For weak anisotropy (WA), the first iteration is usually sufficient for getting accurate results.

3.5 Weak-anisotropy-attenuation parameters

Determination of the complete set of 21 viscoelastic parameters requires measurements of the velocity and attenuation for the *P* and *S* waves. In the case of *P*-wave mesurements only, six parameters related to the *S*-wave propagation (called the *S*-wave related parameters) a_{44}, a_{55}, a_{66}, a_{45}, a_{46} and a_{56} cannot be well resolved (see Svitek *et al.* 2014). Under weak velocity and attenuation anisotropy, the *S*-wave related parameters cannot be determined at all. For this reason, in analogy to WA parameters (see e.g. Pšenčík & Gajewski 1998; Farra & Pšenčík 2003, 2008) we define the so-called weak anisotropy-attenuation (WAA) parameters and modify the inversion scheme to invert for 15 WAA parameters only (see Vavryčuk 2009). Since the reference medium is isotropic, eq. (28) is modified for the *P* wave as follows:

$$\Delta c^2 = \Delta a_{ijkl} n_i n_j n_k n_l, \tag{29}$$

and further rewritten in the form

$$\begin{aligned}\frac{\Delta c^2}{2c_0^2} &= n_1^2 \varepsilon_x + n_2^2 \varepsilon_y + n_3^2 \varepsilon_z + n_2^2 n_3^2 \eta_x + n_1^2 n_3^2 \eta_y + n_1^2 n_2^2 \eta_z \\ &\quad + 2n_2 n_1^3 \varepsilon_{16} + 2n_3 n_1^3 \varepsilon_{15} + 2n_3 n_2^3 \varepsilon_{24} \\ &\quad + 2n_1 n_2^3 \varepsilon_{26} + 2n_1 n_3^3 \varepsilon_{35} + 2n_2 n_3^3 \varepsilon_{34} + 2n_1^2 n_2 n_3 \chi_x \\ &\quad + 2n_1 n_2^2 n_3 \chi_y + 2n_1 n_2 n_3^2 \chi_z\end{aligned} \tag{30}$$

where the complex WAA parameters are defined as

$$\varepsilon_x = \frac{a_{11} - c_0^2}{2c_0^2}, \quad \varepsilon_y = \frac{a_{22} - c_0^2}{2c_0^2}, \quad \varepsilon_z = \frac{a_{33} - c_0^2}{2c_0^2},$$

$$\delta_x = \frac{a_{23} + 2a_{44} - c_0^2}{c_0^2}, \quad \delta_y = \frac{a_{13} + 2a_{55} - c_0^2}{c_0^2},$$

$$\delta_z = \frac{a_{12} + 2a_{66} - c_0^2}{c_0^2},$$

$$\chi_x = \frac{a_{14} + 2a_{56}}{c_0^2}, \quad \chi_y = \frac{a_{25} + 2a_{46}}{c_0^2}, \quad \chi_z = \frac{a_{36} + 2a_{45}}{c_0^2}, \tag{31}$$

$$\varepsilon_{15} = \frac{a_{15}}{c_0^2}, \quad \varepsilon_{16} = \frac{a_{16}}{c_0^2}, \quad \varepsilon_{24} = \frac{a_{24}}{c_0^2}, \quad \varepsilon_{26} = \frac{a_{26}}{c_0^2},$$

$$\varepsilon_{34} = \frac{a_{34}}{c_0^2}, \quad \varepsilon_{35} = \frac{a_{35}}{c_0^2},$$

$$\eta_x = \delta_x - \varepsilon_y - \varepsilon_z, \quad \eta_y = \delta_y - \varepsilon_x - \varepsilon_z, \quad \eta_z = \delta_z - \varepsilon_x - \varepsilon_y,$$

and

$$c_0^2 = \alpha_0^2 \left(1 - \frac{i}{Q_0}\right). \tag{32}$$

Quantities α_0 and Q_0 are the mean real P-wave velocity and P-wave Q-factor in the reference medium.

Knowing the P-wave complex phase velocity c for a set of complex slowness directions $\mathbf{n}$, eq. (30) can be solved for unknown complex WAA parameters using the generalized inversion (Menke 1989). The robustness and accuracy of this inversion will be demonstrated on synthetic data as well as lab measurements in the next sections.

4 NUMERICAL MODELLING

In this section, the inversion for viscoelastic anisotropy is tested on an example of the P wave propagating in a model of an orthorhombic viscoelastic medium (see Tables 1 and 2). The velocity anisotropy corresponds to the Torre Alfina xenolith with parameters taken from Pera *et al.* (2003, their table 3). The attenuation anisotropy is not based on measurements but it is synthetic. The mean P-wave phase velocity of the model is 7.93 km s^{-1} and the P-wave velocity anisotropy is 12.4 per cent. The mean P-wave phase Q-factor is 87.7, and the P-wave Q-factor anisotropy is 84.0 per cent. The density of the Torre Alfina xenolith is 3.31 g cm^{-3}.

The intrinsic phase and ray velocities, attenuations and Q-factors (see Fig. 1) for the synthetic model are calculated using equations from Sections 2.1 and 2.2. The quantities are evaluated in a regular grid of directions with the incidence ranging from $-90°$ to $90°$ and with azimuth from $0°$ to $180°$. The grid step is alternatively $5°$, $10°$, $15°$, $20°$ and $30°$. Hence, in total of 1260, 306, 132, 72 and 30 independent measurements describe the directional variation of the velocity and attenuation. The ray velocity and attenuation values are used for calculating the complex phase velocity (see Section 3.3) which is inverted for the WAA parameters of the medium. The inversion is performed with noise-free and noisy data. Noise is random with a uniform distribution. The noise level is different for the real and imaginary parts of the complex phase velocity c reflecting that the propagation velocity is usually measured with much higher accuracy than attenuation. The noise level for the real part of c varies from 0 to ± 3 per cent with step of 0.2 per cent, and the level for the imaginary part of c varies from 0 to ± 15 per cent with step of 1 per cent. To get statistically robust results, the random noise is generated 100 times and the results of the inversion are averaged over all noise realizations. Since the convergence of the iterative process is quite fast (see Fig. 2), we performed the inversion with six iterations only.

The inversion is run for the velocity and attenuation measured along phase normals (Fig. 3) or along rays (Fig. 4). Fig. 3 shows the maximum errors of the predicted phase velocity V^{phase} and phase attenuation A^{phase} for various grid steps. The maximum value is calculated over all directions and it is further averaged over noise realizations. As expected, the higher the number of input measurements,

Table 1. Elastic and attenuation parameters of the numerical model.

Elastic parameters								
A_{11}^R (km^2 s^{-2})	A_{22}^R (km^2 s^{-2})	A_{33}^R (km^2 s^{-2})	A_{44}^R (km^2 s^{-2})	A_{55}^R (km^2 s^{-2})	A_{66}^R (km^2 s^{-2})	A_{12}^R (km^2 s^{-2})	A_{13}^R (km^2 s^{-2})	A_{23}^R (km^2 s^{-2})
56.74	72.66	62.39	21.21	18.31	20.21	21.36	22.30	22.05
Attenuation parameters								
Q_{11}	Q_{22}	Q_{33}	Q_{44}	Q_{55}	Q_{66}	Q_{12}	Q_{13}	Q_{23}
160	90	120	50	60	65	40	50	60

Notes: The two-index Voigt notation A_{KL}^R and Q_{KL}, $K, L = 1, \ldots, 6$ is used for density-normalized elastic parameters a_{ijkl}^R and quality-factor parameters $q_{ijkl} = -a_{ijkl}^I / a_{ijkl}^R$ (no summation over repeated indexes). The elastic and attenuation parameters not shown in the table are identically zero.

Table 2. P-wave velocity and attenuation anisotropy of the synthetic model.

$\bar{V}^{\mathrm{phase}}$ (km s^{-1})	a_V^{phase} (%)	$\bar{A}^{\mathrm{phase}}$ (s km^{-1})	a_A^{phase} (%)	$\bar{Q}^{\mathrm{phase}}$	a_Q^{phase} (%)
7.93	12.4	7.48×10^{-4}	79.6	87.7	84.0

Notes: $\bar{V}^{\mathrm{phase}}$, $\bar{A}^{\mathrm{phase}}$ and $\bar{Q}^{\mathrm{phase}}$ are the mean P-wave phase velocity, attenuation and Q-factor; a_V^{phase}, a_A^{phase} and a_Q^{phase} are the P-wave phase velocity anisotropy, attenuation anisotropy and Q-factor anisotropy. The anisotropy is calculated as $a = 200\,(U_{\mathrm{MAX}} - U_{\mathrm{MIN}})/(U_{\mathrm{MAX}} + U_{\mathrm{MIN}})$, where U_{MAX} and U_{MIN} are the maximum and minimum values of the respective quantity.

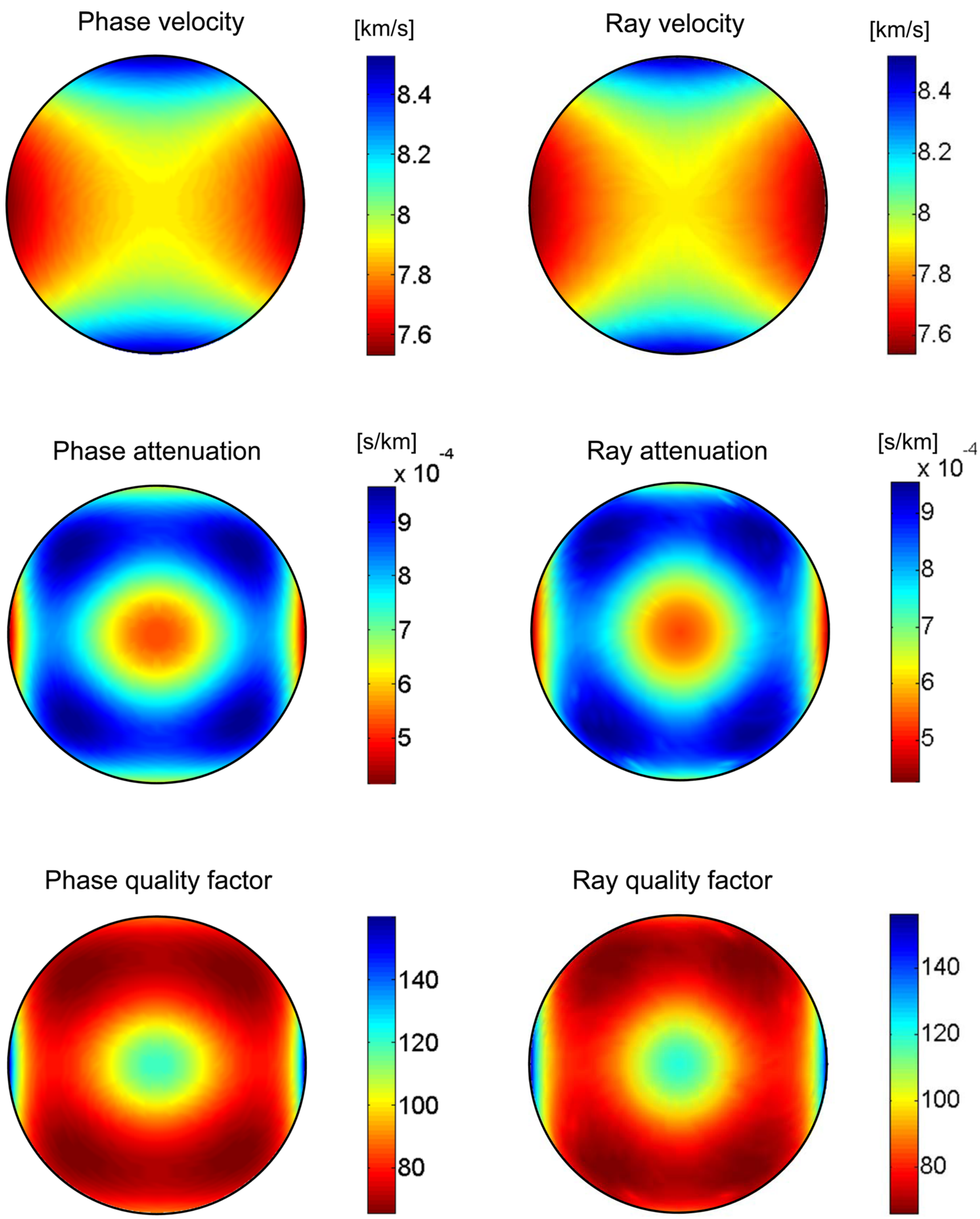

Figure 1. Stereographic plots of the P-wave velocities, attenuations and Q-factors in the model of the Torre Alfina xenolith. Left: phase intrinsic quantities and right: ray intrinsic quantities. For parameters of the model, see Table 1.

the lower the sensitivity of the results to noise. The attenuation errors are significantly higher than the velocity errors because they comprise errors produced by eliminating effects of the inaccurately determined elastic Green's function. Fig. 4 shows similar results as Fig. 3 but for the inversion of ray quantities. The attenuation errors in the inversion of noise-free ray data are due to the recalculation of ray to phase quantities before the inversion of the complex phase velocity c. In the case of a denser grid of ray measurements, this error decreases. For an increasing noise level, the role of the errors due to the recalculation of ray to phase quantities is suppressed. The upper and lower panels in Fig. 5 display the errors in the WAA parameters inverted using the phase and ray quantities for step of 15° in the grid of directions. The numbers identifying the WAA parameters are defined in Table 4 (first two columns). Since the velocity anisotropy is much weaker than the attenuation anisotropy, the real parts of the WAA parameters are more sensitive to noise and thus less accurate than their imaginary parts. Nevertheless, the accuracy of predicted quantities is satisfactory even when inverting data with the highest noise level (Fig. 6). Again, the accuracy of the results is worse for the inversion of ray quantities (Figs 1 and 6) because of the necessity to recalculate the ray to phase quantities before the inversion.

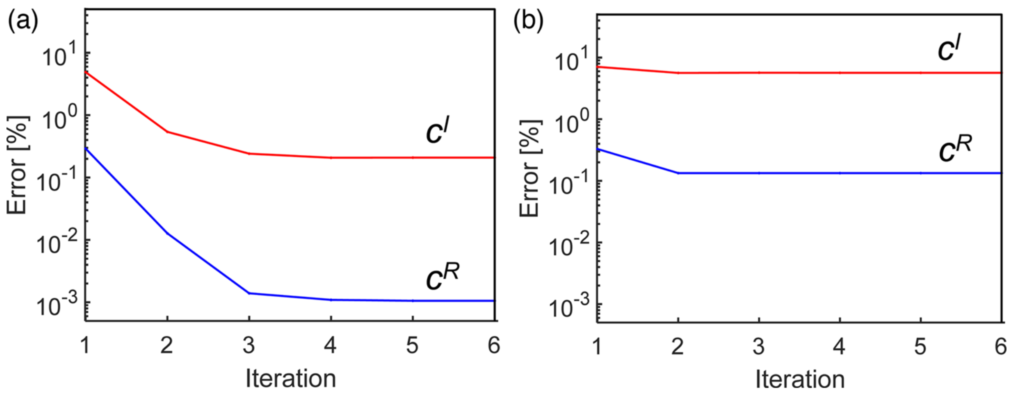

Figure 2. The relative error between the true and predicted complex phase velocity as a function of the number of iterations of the inversion. The error is calculated as the maximum over all directions. The inversion is run for (a) the phase quantities and (b) the ray quantities. Blue/red: the real/imaginary part of the complex phase velocity. The higher errors in (b) than in (a) are due to the recalculation of ray to phase quantities in a sparse grid of directions (step of 15°) before the inversion.

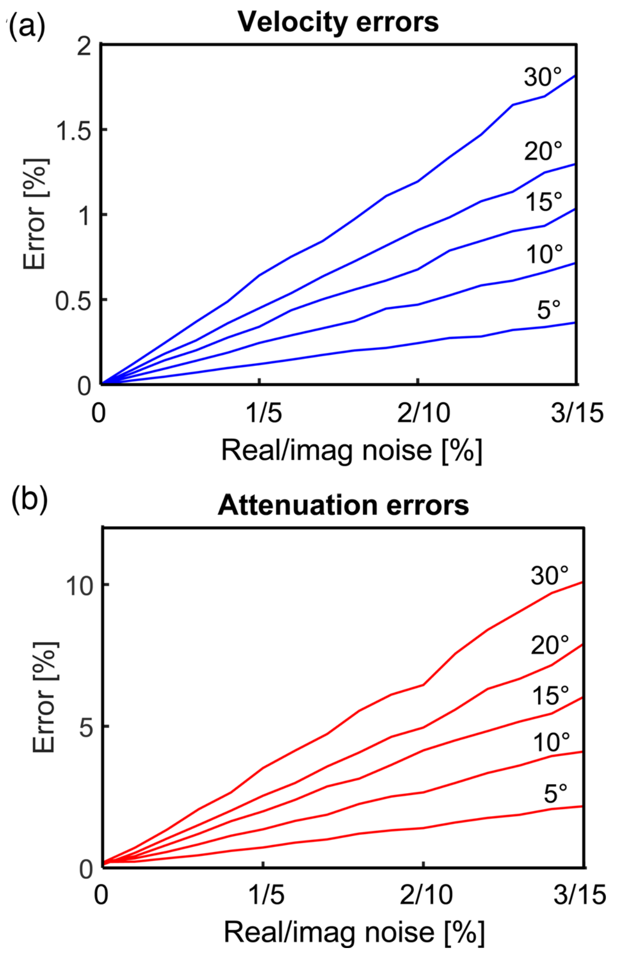

Figure 3. Errors of the predicted (a) phase velocity and (b) attenuation using the inversion of phase quantities. The errors for several alternative grid steps (5°, 10°, 15°, 20° and 30°) are displayed as a function of noise in input data. The real part of noise (0–3 per cent) is five times lower than its imaginary part (0–15 per cent) expressing higher uncertainties in measurements of signal amplitudes than in traveltimes.

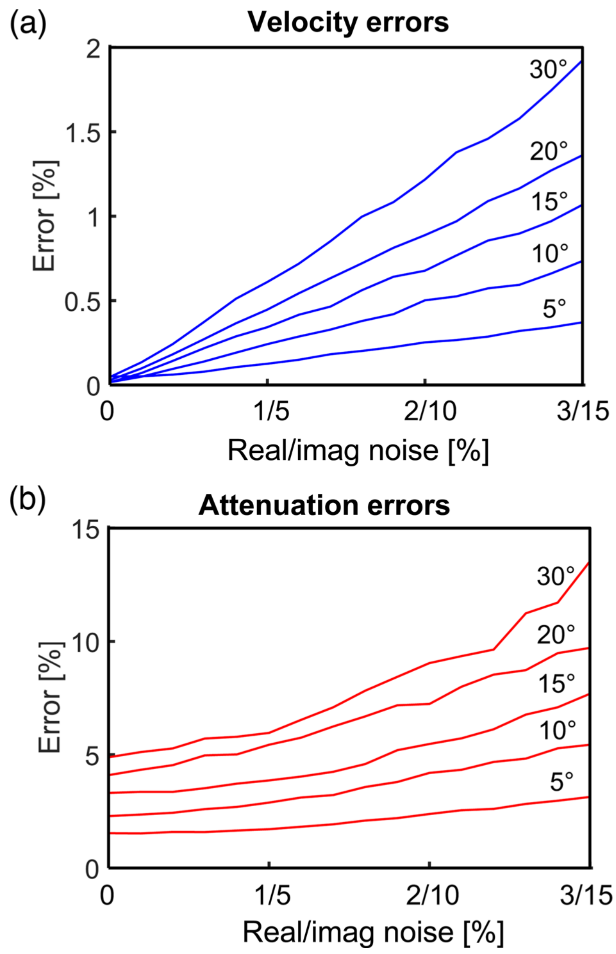

Figure 4. Errors of the predicted (a) phase velocity and (b) attenuation using the inversion of ray quantities. The errors for several alternative grid steps (5°, 10°, 15°, 20° and 30°) are displayed as a function of noise in input data. The real part of noise (0–3 per cent) is five times lower than its imaginary part (0–15 per cent) expressing higher uncertainties in measurements of signal amplitudes than in traveltimes.

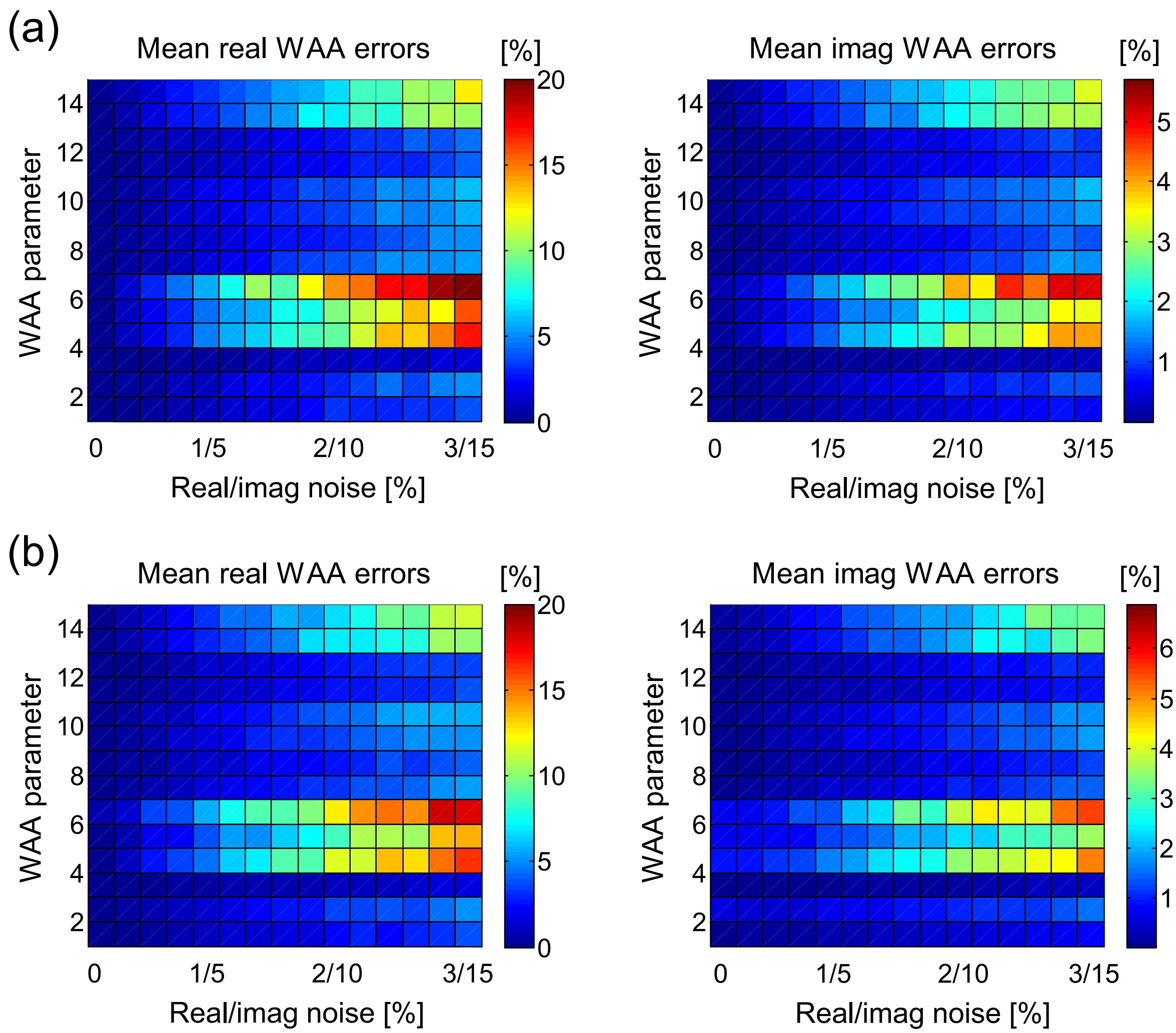

Figure 5. Errors of the real (left) and imaginary (right) parts of the retrieved weak-anisotropy-attenuation (WAA) parameters. The errors are displayed as a function of noise in input data. The inversion is run for (a) the phase quantities and (b) the ray quantities in a grid of directions with step of 15°.

5 LABORATORY MEASUREMENTS

5.1 Setup of the experiment

The determination of viscoelastic anisotropy is exemplified using an experimental facility that allows a measurement of the *P*-wave ray velocities and *P*-wave amplitudes on spherical rock samples. A diameter of the analysed rock sample is 45.5 mm but the equipment is capable of measuring also spherical samples of other diameters using specially designed arms. These arms enable insertion of a setting ring to adapt a different diameter of individual spherical samples (see Fig. 7). The sample was measured at room temperature being exposed to confining pressures of 0.1 and 20 MPa. Two piezoceramic sensors had a plain contact surface that resulted in a point contact between the sensor and the sphere.

The ultrasonic signals were excited and recorded by a piezoceramics sensor pair with a resonant frequency of 2 MHz. The equipment allows for an ultrasonic sounding of rock samples in 132 independent directions with a pair of the *P*-wave sensors where both transmitter and receiver are polarized along the radial direction. The waveforms of ultrasonic signals were recorded using an A/D convertor with the dynamic range of 8 bits and with the sampling frequency of 100 MHz. Each waveform was recorded 10 times and then averaged in order to reduce noise. The sensitivity of the convertor was set up to record individual signals without any distortion and with the maximum possible dynamics. During the measurement, the point contact between the spherical sample and the transducers was established by a metal spring that acted by constant force at every direction. Transform oil was used as pressure medium.

5.2 Rock sample

We measured a sample of serpentinite from Val Malenco, Northern Italy, which comes from the block of serpentinite with the Kiel sample number 987 (Kern *et al*. 2015). At ambient conditions, the bulk density of the serpentinite derived from the volume and the mass of the sample sphere is 2.71 g cm^{-3}. The constituent minerals are 83 vol.% antigorite, 13 vol.% olivine, 2 vol.% magnetite and 2 vol.% chromite. The average grain size is about 200 μm. The porosity is rather low; the volume compaction of 1.63 per cent

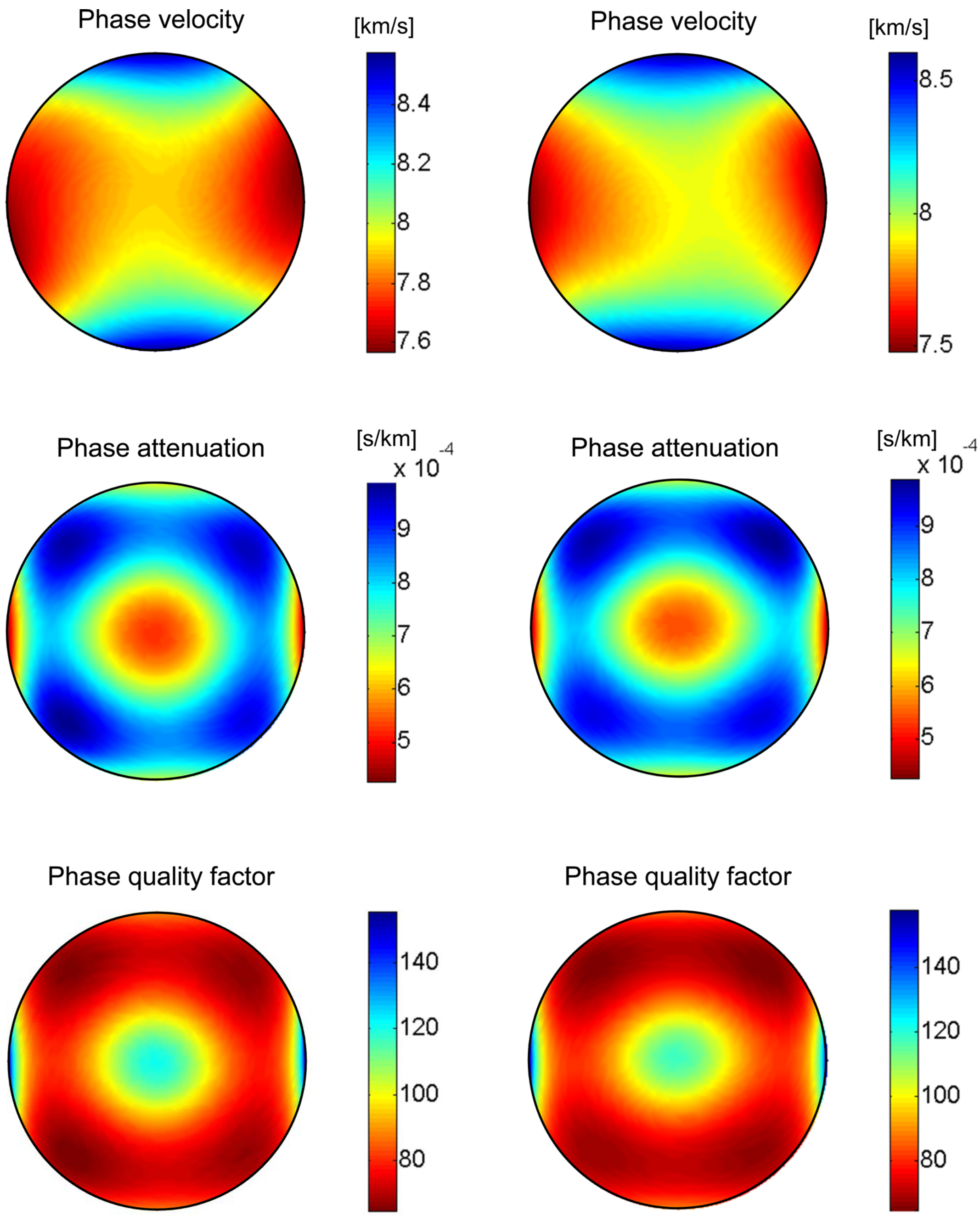

Figure 6. Stereographic plots of the predicted *P*-wave phase velocities, attenuations and *Q*-factors in the model of the Torre Alfina xenolith retrieved by the inversion in a grid of directions with step of 15°. Left: inversion of the phase quantities and right: inversion of the ray quantities. The noise level was up to ±3 and ±15 per cent in the real and imaginary parts of the complex phase velocity, respectively.

represents mainly the crack porosity. The sample displays a pronounced lattice preferred orientation of antigorite, that has been documented by 13.2 and 13.6 m.r.d. maxima for (001) pole figures in Kern *et al*. (2015), values that are consistent with other foliated serpentinites. To protect the pore space against the oil, the spherical surface of the sample was covered by a thin layer of an epoxy resin.

The *P*- and *S*-wave velocity and attenuation anisotropy of this rock has also been studied by Kern *et al*. (1997). In that study, the authors used a cubic sample with axes of the cube referring to macroscopic fabric coordinates: *x* parallel to the lineation, *y* normal to the lineation within the foliation plane and *z* normal to the foliation plane. The velocity and attenuation has been measured as a function of pressure up to 600 MPa and temperature up to 600 °C. The most prominent changes have been detected for pressure ranging from 0 to 100 MPa related to the closure of grain boundary cracks. While the mean velocity slightly increased, the mean attenuation remarkably decreased with increasing pressure (see Kern *et al*. 1997, their fig. 9a). Obviously, this dependence must be visible also in the measurements performed on the spherical sample in this paper.

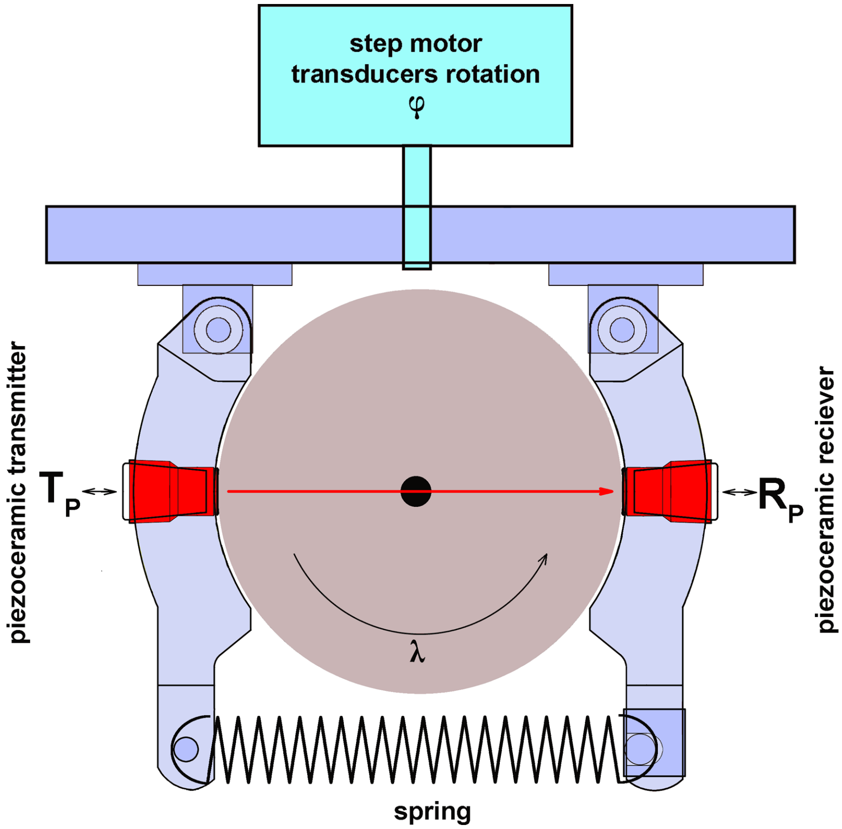

Figure 7. The experimental setup and measurement geometry shown in the horizontal plane; TP and RP are the radial transmitter and receiver, respectively (mostly generating and sensitive to the *P* waves). The axis of rotation is vertical. The red colour marks the setting ring for adapting a different diameter of individual spherical samples.

5.3 Data processing

The ultrasonic measurements provide waveforms in 132 independent directions (see Fig. 8). The waveforms consist of a direct *P* wave followed by scattered coda waves produced by multiple reflections and conversions at the surface of the sample. As a consequence, the complete waveforms are complex and difficult to interpret (Fig. 8a). Nevertheless, the analysis of the direct *P* wave is rather simple because the secondary reflections arrive at times sufficient for separation of the direct *P* wave. The *P*-wave onset is usually noise-free and well distinguished and its determination can be performed using an automatic picking algorithm (Allen 1982; Sedlák *et al*. 2009; Svitek *et al*. 2010). The amplitude of the *P* wave is defined as the amplitude of the first maximum (or minimum) after the *P*-wave arrival and its automatic measurement is reliable with an error less than few samples (see Fig. 9).

Since the piezoceramics pair of sensors used for emitting and receiving the ultrasonic waves are planar, they touch the spherical sample at an area of about 2 × 2 mm or less. Since the size of the contact is much smaller than the radius of the sample, the contact between the sensors and the rock sample is considered to be point-like. Consequently, the wave front of excited waves is not planar but curved and the velocity and amplitude of the signals are not measured along a phase normal but along a ray. Completing measurements of the traveltime and amplitude of the ultrasonic signal propagating through the sample in all directions, we construct a directional dependence of the ray velocity and ray amplitude for both pressure levels (see Fig. 10). As expected, the average velocity is slightly higher for confining pressure of 20 MPa because of a closure of cracks (see Table 3). This effect is even more pronounced in amplitudes indicating distinctly lower attenuation at this pressure level. The directional patterns of velocities and amplitudes are, however, similar for both pressure levels. Only, the amplitude variations seem to be slightly rotated relative to each other.

5.4 Results

The determination of parameters of viscoelastic anisotropy from measured velocities and amplitudes is performed in the following steps. First, the elastic anisotropy must be calculated from the directional variation of ray velocities. The procedure is quite analogous to that described in Section 3.4, but all quantities are real in the inversion. Second, the radiation pattern of a point source in elastic anisotropy is calculated (see Section 3.2). Third, the directionally dependent amplitudes of the signal emitted by the source and the amplitudes recorded at the receiver (Figs 8 and 9) are used for calculating the corrected amplitude decay along a ray and the ray attenuation (see Section 3.2). Fourth, an additional effect of a thin layer of an epoxy resin on the surface of the sample must be taken into account. The layer of the epoxy resin causes a uniform diminution of amplitudes in all directions and thus affects the scale of the determined ray attenuation and *Q*-factor. Therefore, the scale was adjusted by measurements of Kern *et al*. (1997) carried out for the same rock in the directions of the symmetry axes. The resultant ray attenuation and *Q*-factor patterns (see Fig. 11 and Table 3)

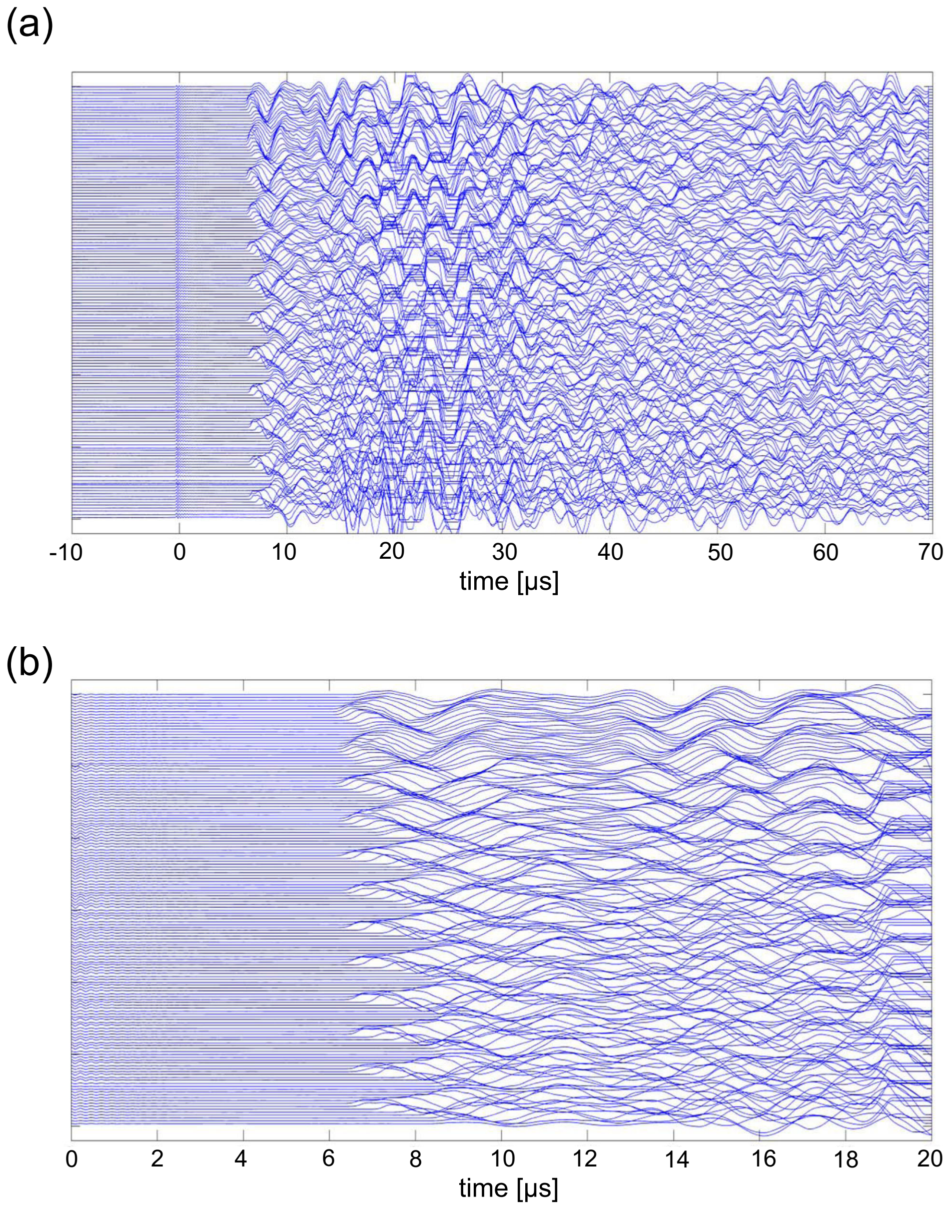

Figure 8. Ultrasonic signals observed for the serpentinite sample at confining pressure of 0.1 MPa. The waveforms are recorded in all directions at two different timescales. The origin of the timescale corresponds to the excitation time of the signal.

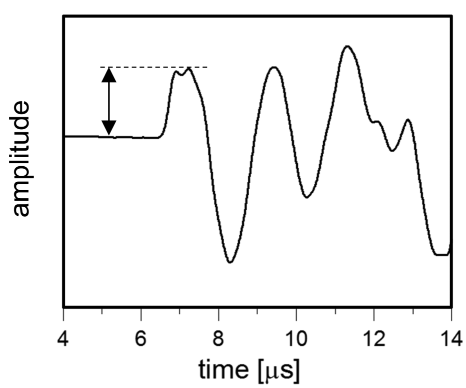

Figure 9. Example of one trace taken from the set in Fig. 8 showing how the amplitude of the direct P wave was measured.

confirm a remarkable decrease of attenuation for the pressure of 20 MPa compared to the atmospheric pressure. However, the attenuation anisotropy and the Q-factor anisotropy increase. The increase of anisotropy strength indicates that the effects of aligned structure elements and inhomogeneities are more pronounced under confining pressure. Finally, the phase velocity and attenuation were calculated from the ray quantities according to Section 3.3 (see Fig. 12) and inverted for the parameters of viscoelastic anisotropy (see Table 4).

The predicted phase velocity, attenuation and Q-factor are displayed in Fig. 13. The predicted quantities are very similar to the input phase data indicating that the inversion was successful. The basic pattern of the predicted quantities at two pressure levels is also similar with some minor differences in attenuation and Q-factor. In particular, we observe a clockwise rotation of attenuation and Q-factors patterns by about 30°. Since the velocity pattern is unchanged for both pressure levels, the difference in attenuation

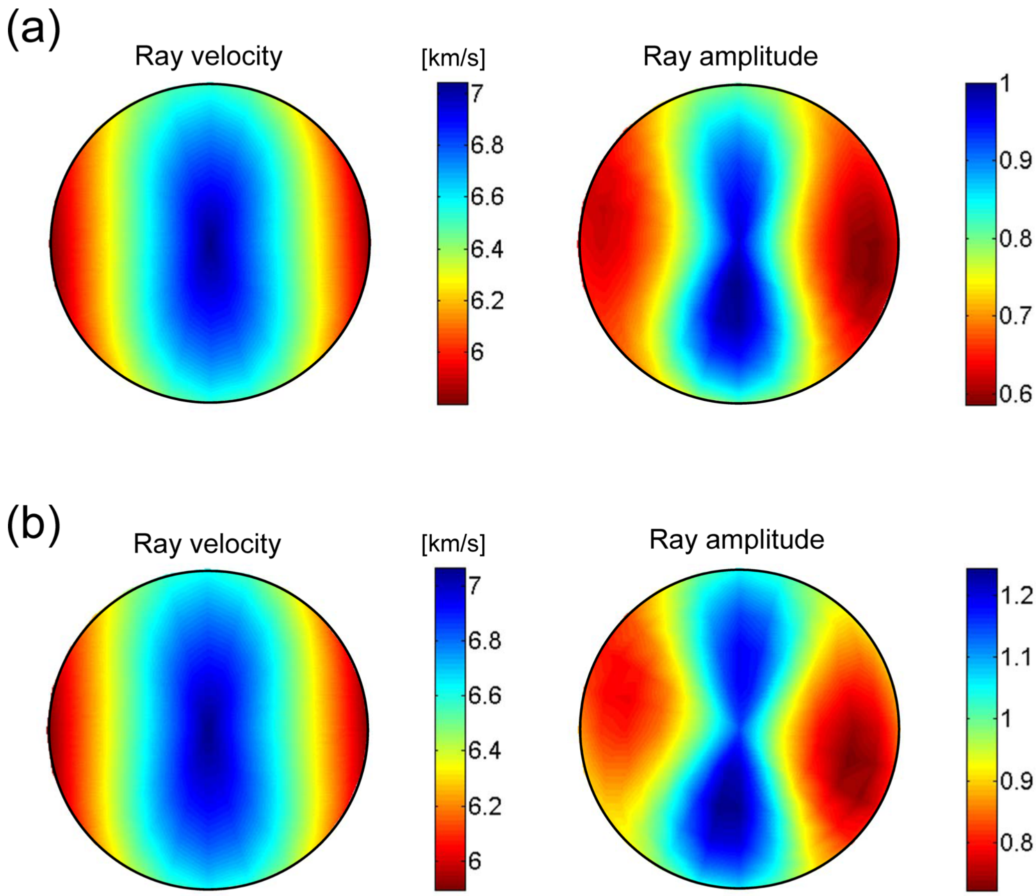

Figure 10. Directional variations of ray velocity and ray amplitude measured for the serpentinite sample at confining pressure of (a) 0.1 MPa and (b) 20 MPa. The amplitudes in (a) and (b) are normalized to the maximum amplitude measured at 0.1 MPa.

Table 3. *P*-wave velocity and attenuation anisotropy of the serpentinite rock sample.

Pressure (MPa)	$\bar{V}^{\mathrm{phase}}$ (km s^{-1})	a_V^{phase} (%)	$\bar{A}^{\mathrm{phase}}$ (s km^{-1})	a_A^{phase} (%)	$\bar{Q}^{\mathrm{phase}}$	a_Q^{phase} (%)
0.1	6.51	22.9	11.0×10^{-4}	33.2	69.5	16.6
20	6.57	21.5	8.8×10^{-4}	38.5	92.1	32.1

Notes: For the definition and meaning of the quantities, see Table 2.

and Q-factors could not be produced by a misorientation of the sample in the two measurements, but it should be a real stress-induced effect. This indicates that anelastic properties of rocks are more sensitive to confining pressure than their elastic properties.

6 DISCUSSION AND CONCLUSIONS

An accurate and correct determination of anisotropic attenuation of rocks in laboratory is not an easy task. It needs an experimental facility that allows for measurement of the traveltime and amplitude decay of waves propagating along a dense grid of directions. The determination of viscoelastic parameters is simpler if we use measurements of plane waves than of waves generated by a point source. For plane waves propagating through the rock sample, we measure the traveltime and amplitude decay along the phase normal. Subsequently, we calculate the real phase velocity and phase attenuation, construct the complex phase velocity and invert for viscoelastic anisotropy.

For waves generated by point sources, we measure the traveltime and amplitudes along a ray. In order to calculate the amplitude decay and subsequently the ray attenuation, we have to measure wave amplitudes at two points along a ray. This can be realized by measuring amplitudes for two samples of a different size or by measuring amplitudes just for one sample provided we know the amplitude of the wave emitted at the source. In this case, however, the amplitude at the source must be corrected for geometrical spreading and for the radiation pattern of a point source in anisotropic media. Knowing the ray velocity and ray attenuation, we can construct the complex energy velocity. This velocity is further recalculated to the complex phase velocity using the polar reciprocity relation. After that we can invert for the viscoelastic anisotropy.

Using measurements of P waves we cannot determine the complete tensor of viscoelastic parameters. The six of the 21 viscoelastic parameters related to propagation of the S waves cannot be determined. The inversion for viscoelastic anisotropy is non-linear, but it can be linearized. The linearization and elimination of the S-wave related parameters can conveniently be performed using the so-called WAA parametrization. Since the inversion is run in iterations, it is applicable even to strong attenuation anisotropy.

Numerical tests on synthetic data proved that the inversion for the WAA parameters worked well. The convergence of the iterative

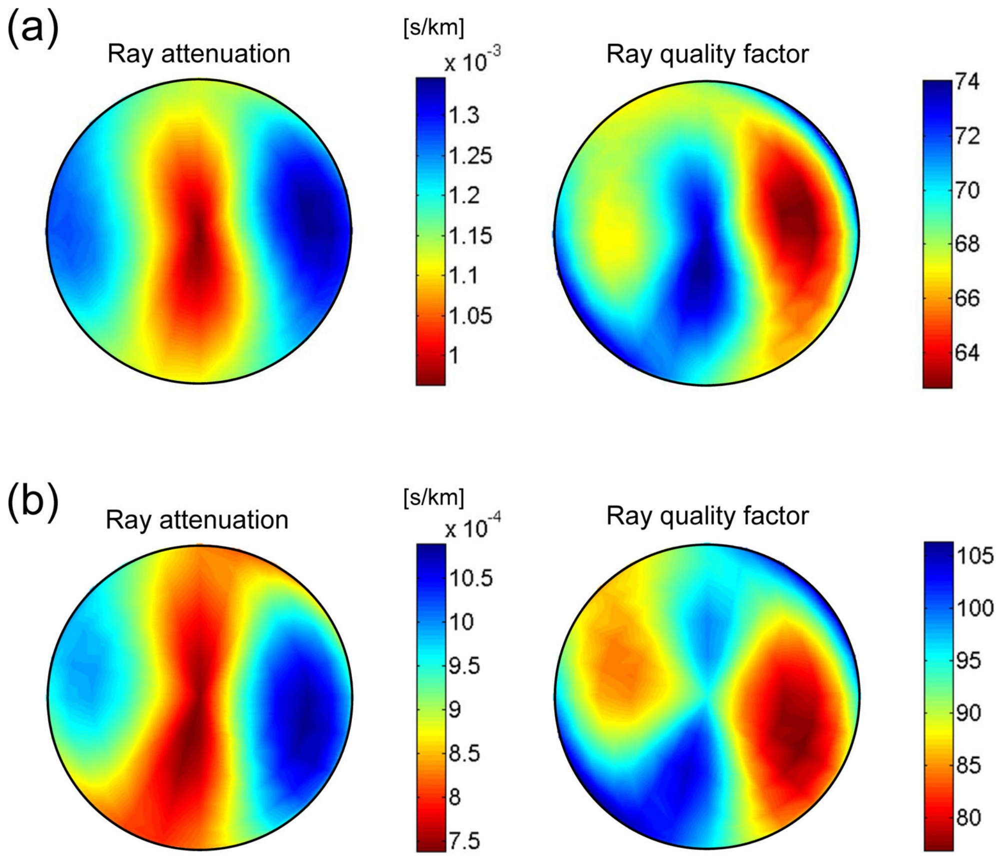

Figure 11. The ray attenuation and ray quality factor for the serpentinite sample at confining pressure of (a) 0.1 MPa and (b) 20 MPa. The attenuation and quality factor are determined from the ray amplitudes shown in Fig. 10 and from the radiation pattern of the point source in the anisotropic serpentinite rock (see Section 3.2).

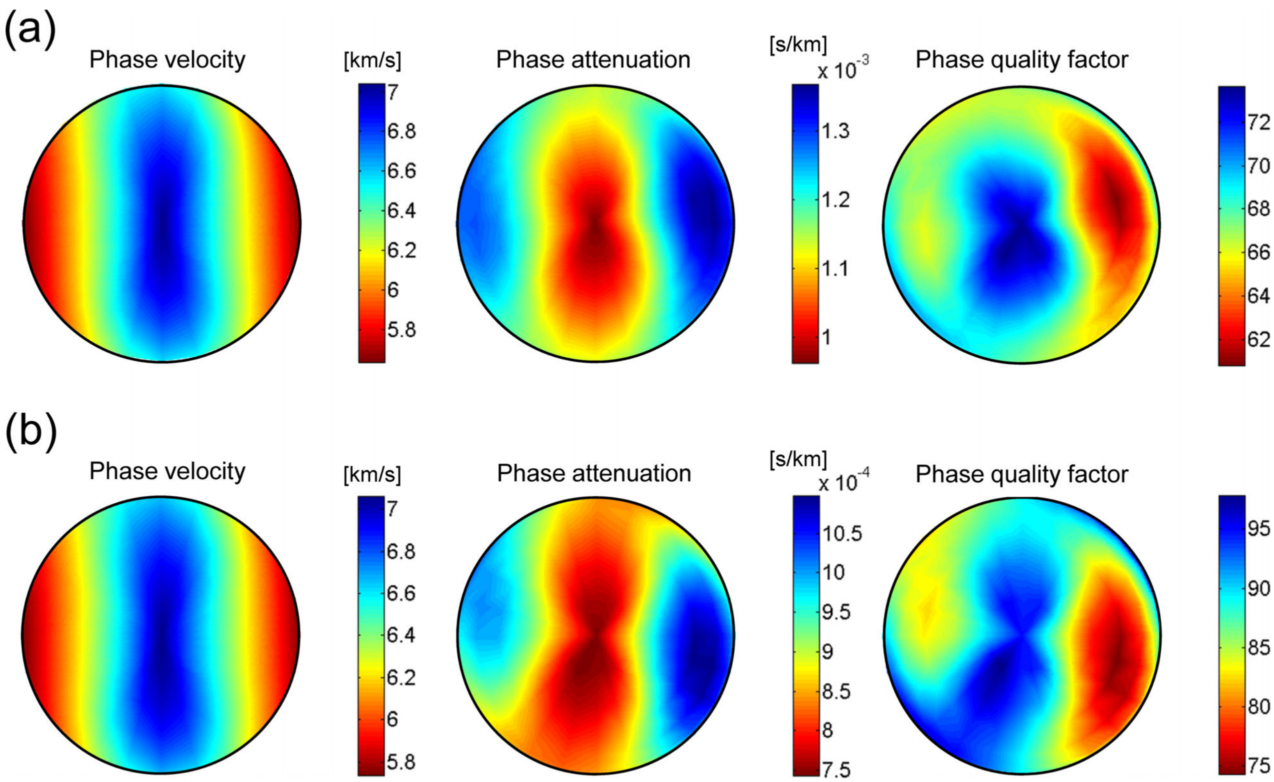

Figure 12. The phase velocity, attenuation and quality factor for the serpentinite sample at confining pressure of (a) 0.1 MPa and (b) 20 MPa. The phase quantities were calculated from the measured ray quantities and served as the input data for the inversion for parameters of viscoelastic anisotropy.

Table 4. WAA parameters of the serpentinite rock sample.

No.	WAA	Pressure 0.1 MPa		Pressure 20 MPa	
		Real part (10^{-3})	Imaginary part (10^{-4})	Real part (10^{-3})	Imaginary part (10^{-4})
1	ε_x	−115.4	−54.1	−109.9	−41.5
2	ε_y	13.8	−76.4	18.1	−58.3
3	ε_z	87.0	−80.7	79.0	−61.9
4	η_x	16.5	−11.1	28.9	−6.1
5	η_y	−151.7	−19.8	−148.2	−28.3
6	η_z	1.8	−1.2	−1.1	−4.8
7	ε_{16}	−7.9	2.4	−5.1	2.9
8	ε_{15}	4.9	−2.7	4.1	−2.3
9	ε_{24}	−4.4	0.1	−5.1	0.8
10	ε_{26}	−9.9	4.1	−7.8	5.7
11	ε_{35}	3.6	−4.0	3.6	−4.7
12	ε_{34}	−5.2	−1.4	−5.7	0.0
13	χ_x	−1.6	−0.2	−3.3	1.4
14	χ_y	6.2	−4.9	7.9	−7.7
15	χ_z	3.5	−5.7	7.7	5.8

process was quite fast. The accuracy of the retrieved parameters was higher if the phase velocity and attenuation were inverted. Utilizing ray velocity and attenuation worked slightly worse because of the necessity of recalculating the ray to phase quantities before the inversion. In both inversions, the accuracy of the individual WAA parameters significantly varied. The lowest accuracy was achieved for parameters η_x, η_y and η_z reflecting a rather low sensitivity of the *P*-wave velocity and attenuation to them.

The applicability of the proposed methods was exemplified by determining anisotropic attenuation of a serpentinite rock from Val Malenco, Northern Italy. The ray velocity and ray attenuation were measured on a spherical sample of the rock with the diameter of 45.5 mm in 132 independent directions at the room temperature and under two pressure levels: 0.1 and 20 MPa. First, elastic anisotropy of the rock sample was determined and then attenuation anisotropy was inverted for. To our knowledge, the results obtained for the serpentinite rock sample represent the first accurately determined triclinic anisotropic attenuation from lab measurements. The measurements confirmed that anisotropic attenuation is remarkably sensitive to confining pressure. Since cracks are closing with increasing pressure, attenuation decreases. If cracks are preferentially oriented, the crack closure can diminish also the velocity anisotropy. However, changes in pressure acting on a rock with preferentially oriented crack systems can also induce changes in the directional variation of attenuation and a rotation of anisotropy axes.

We applied the proposed method to determination of anisotropic attenuation of a dry rock sample from lab measurements, but the applicability of the approach is broader. The approach can be applied to measurements of saturated rock samples to study fluid-driven attenuation and fluid flow in rocks. Attenuation effects similar to those measured in the lab will probably be observed also in seismic field experiments. Since the Earth's crust and the mantle are anisotropic and attenuating, future detailed seismological tomographic studies will include effects of anisotropic attenuation. Such studies can advantageously apply the model of viscoelastic anisotropy and follow the inversion schemes presented in this paper after adapting them to a different configuration and scale of the experiment and to a different frequency range of studied waves.

ACKNOWLEDGEMENTS

We thank Jörg Renner, Georg Dresen, José Carcione and two anonymous reviewers for their helpful comments, and Prof H. Kern for providing us with the serpentinite sample. The technical help of

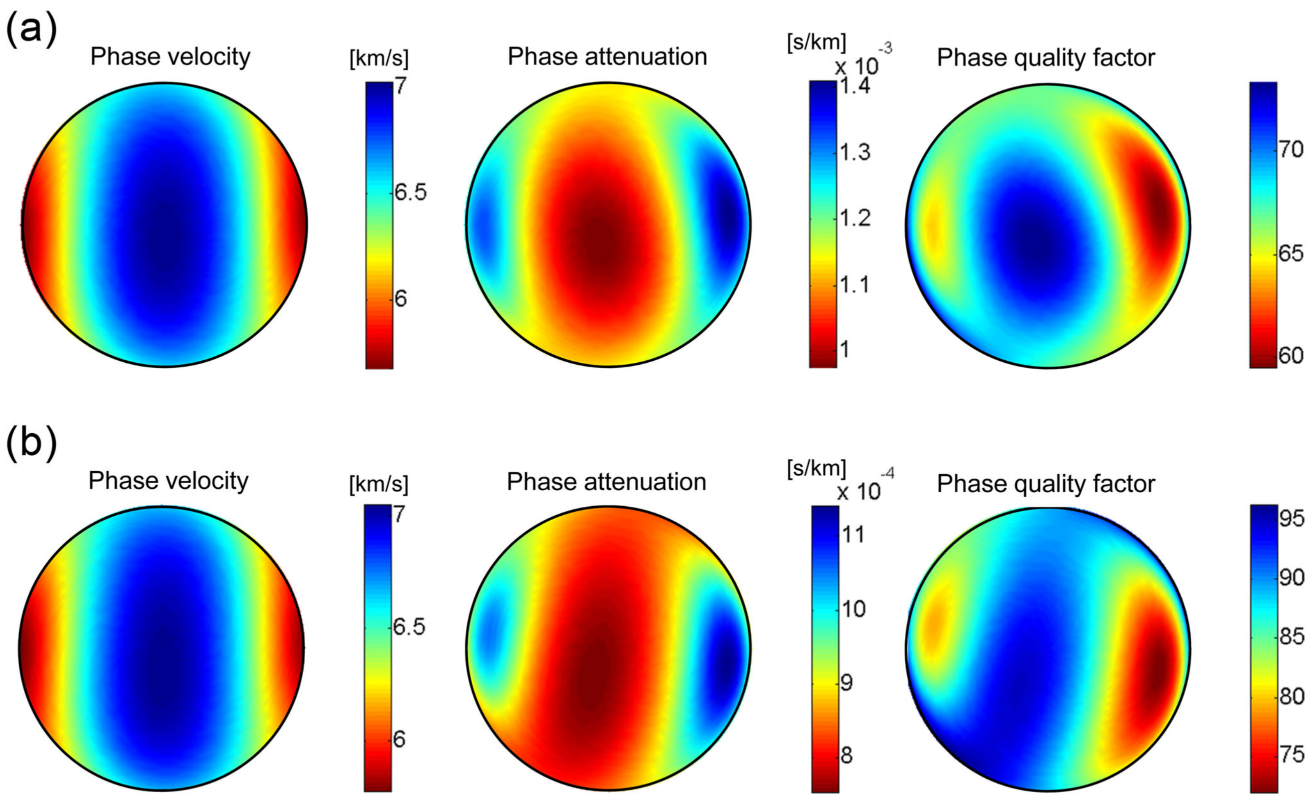

Figure 13. The predicted phase velocity, attenuation and quality factor for the serpentinite sample at confining pressure of (a) 0.1 MPa and (b) 20 MPa. The phase quantities were calculated using the weak-anisotropy-attenuation (WAA) parameters retrieved by the inversion.

V. Filler and V. Nemejovský is greatly appreciated. This study was supported by the Grant Agency of the Czech Republic, projects P210/12/1491 and 16-19751J, by the Ministry of Education, project Kontakt II LH13102 and by The Czech Academy of Sciences, project RVO 67985831.

REFERENCES

Allen, R., 1982. Automatic phase pickers: their present use and future prospects, *Bull. seism. Soc. Am.,* **72**(6), S225–S242.

Auld, B.A., 1973. *Acoustic Fields and Waves in Solids,* Wiley.

Babuška, V. & Cara, M., 1991. *Seismic Anisotropy in the Earth,* Kluwer.

Borcherdt, R.D., 2009. *Viscoelastic Waves in Layered Media,* Cambridge Univ. Press.

Burton, N., 2007. *Rock Quality, Seismic Velocity, Attenuation and Anisotropy,* Taylor & Francis.

Carcione, J.M., 1990. Wave propagation in anisotropic linear viscoelastic media: theory and simulated wavefields, *Geophys. J. Int.,* **101,** 739–750.

Carcione, J.M., 1993. Seismic modeling in viscoelastic media, *Geophysics,* **58,** 110–120.

Carcione, J.M., 1994. Wavefronts in dissipative anisotropic media, *Geophysics,* **59,** 644–657.

Carcione, J.M., 2000. A model for seismic velocity and attenuation in petroleum source rocks, *Geophysics,* **65,** 1080–1092.

Carcione, J.M., 2014. *Wave Fields in Real Media: Theory and Numerical Simulation of Wave Propagation in Anisotropic, Anelastic, Porous and Electromagnetic Media,* 3rd edn (extended and revised), Elsevier.

Carcione, J.M., Quiroga-Goode, G. & Cavallini, F., 1996. Wavefronts in dissipative anisotropic media: comparison of the plane wave theory with numerical modeling, *Geophysics,* **61,** 857–861.

Carcione, J.M. & Ursin, B., 2016. On Fermat principle and Snell law in lossy anisotropic media, *Geophysics,* **3,** T107–T116.

Červený, V., 2001. *Seismic Ray Theory,* Cambridge Univ. Press.

Červený, V. & Pšenčík, I., 2005. Plane waves in viscoelastic anisotropic media—I. Theory, *Geophys. J. Int.,* **161,** 197–212.

Chapman, M., 2003. Frequency-dependent anisotropy due to meso-scale fractures in the presence of equant porosity, *Geophys. Prospect.,* **51**(5), 369–379.

Farra, V. & Pšenčík, I., 2003. Properties of the zeroth-, first-, and higher-order approximations of attributes of elastic waves in weakly anisotropic media, *J. acoust. Soc. Am.,* **114,** 1366–1378.

Farra, V. & Pšenčík, I., 2008. First-order ray computations of coupled *S* waves in inhomogeneous weakly anisotropic media, *Geophys. J. Int.,* **173,** 979–989.

Fouch, M.J. & Rondenay, S., 2006. Seismic anisotropy beneath stable continental interiors, *Phys. Earth planet. Inter.,* **158**(2–4), 292–320.

Gajewski, D. & Pšenčík, I., 1992. Vector wavefields for weakly attenuating anisotropic media by the ray method, *Geophysics,* **57,** 27–38.

Hanyga, A. & Seredynska, M., 2000. Ray tracing in elastic and viscoelastic media, *Pure appl. Geophys.,* **157,** 679–717.

Hearn, D.J. & Krebes, E.S., 1990. On computing ray-synthetic seismograms for anelastic media using complex rays, *Geophysics,* **55**(4), 422–432.

Helbig, K., 1994. *Foundations of Anisotropy for Exploration Seismics,* Pergamon.

Hosten, B., Deschamps, M. & Tittmann, B.R., 1987. Inhomogeneous wave generation and propagation in lossy anisotropic solids: application to the characterization of viscoelastic composite materials, *J. acoust. Soc. Am.,* **82,** 1763–1770.

Johnston, D.H. & Toksöz, M.N., 1980. Ultrasonic *P* and *S* wave attenuation in dry and saturated rocks under pressure, *J. geophys. Res.,* **85**(B2), 925–936.

Kern, H., Liu, B. & Popp, T., 1997. Relationship between anisotropy of *P* and *S* wave velocities and anisotropy of attenuation in serpentinite and amphibolite, *J. geophys. Res.,* **102,** 3051–3065.

Kern, H., Lokajíček, T., Svitek, T. & Wenk, H.R., 2015. Seismic anisotropy of serpentinite from Val Malenco, Italy, *J. geophys. Res.,* **120**(6), 4113–4129.

Kim, D.-C., Katahara, K.W. & Manghnani, M.H., 1983. Velocity and attenuation anisotropy in deep-see carbonate sediments, *J. geophys. Res.,* **88,** 2337–2343.

Kravtsov, Yu.A., Forbes, G.W. & Asatryan, A.A., 1999. Theory and applications of complex rays, in *Progress in Optics,* Vol. 39, pp. 3–62, ed. Wolf, E., Elsevier, Amsterdam.

Lipschutz, S., 1969. *Theory and Problems of Differential Geometry,* McGraw-Hill.

Lokajíček, T., Kern, H., Svitek, T. & Ivankina, T., 2014. 3D velocity distribution of *P*- and *S*-waves in a biotite gneiss, measured in oil as the pressure medium: comparison with velocity measurements in a multi-anvil pressure apparatus and with texture-based calculated data, *Phys. Earth planet. Inter.,* **231,** 1–15.

Menke, W., 1989. *Geophysical Data Analysis: Discrete Inverse Theory,* Academic Press.

Mensch, T. & Rasolofosaon, P., 1997. Elastic-wave velocities in anisotropic media of arbitrary symmetry—generalization of Thomsen's parameters ε, δ and γ, *Geophys. J. Int.,* **128,** 43–64.

Mukerji, T. & Mavko, G., 1994. Pore fluid effects on seismic velocity in anisotropic rocks, *Geophysics,* **59**(2), 233–244.

Pera, E., Mainprice, D. & Burlini, L., 2003. Anisotropic seismic properties of the upper mantle beneath the Torre Alfina area (Northern Apennines, Central Italy), *Tectonophysics,* **370,** 11–30.

Pros, Z., Lokajíček, T. & Klíma, K., 1998. Laboratory approach to the study of elastic anisotropy on rock samples, *Pure appl. Geophys.,* **151,** 619–629.

Pros, Z., Lokajíček, T., Přikryl, R. & Klíma, K., 2003. Direct measurement of 3D elastic anisotropy on rocks from the Ivrea zone (Southern Alps, NW Italy), *Tectonophysics,* **370,** 31–47.

Pšenčík, I. & Gajewski, D., 1998. Polarization, phase velocity and NMO velocity of qP waves in arbitrary weakly anisotropic media, *Geophysics,* **63,** 1754–1766.

Pšenčík, I. & Vavryčuk, V., 2002. Approximate relation between the ray vector and wave normal in weakly anisotropic media, *Stud. Geophys. Geod.,* **46,** 793–807.

Rasolofosaon, P., 2010. Generalized anisotropy parameters and approximations of attenuations and velocities in viscoelastic media of arbitrary anisotropy type—theoretical and experimental aspects, *Geophys. Prospect.,* **58**(4), 637–655.

Romanowicz, B., 2003. Global mantle tomography: progress status in the past 10 years, *Ann. Rev. Earth planet. Sci.,* **31,** 303–328.

Savage, M.K., 1999. Seismic anisotropy and mantle deformation: what have we learned from shear wave splitting? *Rev. Geophys.,* **37**(1), 65–106.

Sedlák, P., Hirose, Y., Khan, S.A., Enoki, M. & Sikula, J., 2009. New automatic localization technique of acoustic emission signals in thin metal plates, *Ultrasonics,* **49**(2), 254–262.

Shuvalov, A.L. & Scott, N.H., 1999. On the properties of homogeneous viscoelastic waves, *Q. J. Mech. appl. Math.,* **52,** 405–417.

Stanchits, S., Lockner, D.A. & Ponomarev, A.V., 2003. Anisotropic changes in *P*-wave velocity and attenuation during deformation and fluid infiltration of granite, *Bull. seism. Soc. Am.,* **93**(4), 1803–1822.

Svitek, T., Rudajev, V. & Petružálek, M., 2010. Determination of *P*-wave arrival time of acoustic events, *Acta Montan. Slov.,* **15**(2), 145–151.

Svitek, T., Vavryčuk, V., Lokajíček, T. & Petružálek, M., 2014. Determination of elastic anisotropy of rocks from *P*- and *S*-wave velocities: numerical modelling and lab measurements, *Geophys. J. Int.,* **199**(3), 1682–1697.

Vavryčuk, V., 2003. Parabolic lines and caustics in homogeneous weakly anisotropic solids, *Geophys. J. Int.,* **152,** 318–334.

Vavryčuk, V., 2007a. Asymptotic Green's function in homogeneous anisotropic viscoelastic media, *Proc. R. Soc. A,* **463,** 2689–2707.

Vavryčuk, V., 2007b. Ray velocity and ray attenuation in homogeneous anisotropic viscoelastic media, *Geophysics,* **72,** D119–D127.

Vavryčuk, V., 2008a. Real ray tracing in anisotropic viscoelastic media, *Geophys. J. Int.,* **175,** 617–626.

Vavryčuk, V., 2008b. Velocity, attenuation and quality factor in anisotropic viscoelastic media: a perturbation approach, *Geophysics,* **73**(5), D63–D73.

Vavryčuk, V., 2009. Weak anisotropy-attenuation parameters, *Geophysics,* **74**(5), WB203–WB213.

Vavryčuk, V., 2010. Behaviour of rays at interfaces in anisotropic viscoelastic media, *Geophys. J. Int.,* **181,** 1665–1677.

Vavryčuk, V., 2012. On numerically solving the complex eikonal equation using real ray-tracing methods: a comparison with the exact analytical solution, *Geophysics,* **77,** T109–T116.

Vavryčuk, V., 2015. Determination of parameters of viscoelastic anisotropy from ray velocity and ray attenuation: theory and numerical modeling, *Geophysics,* **80**(3), C59–C71.

Wenzlau, F., Altmann, J.B. & Müller, T.M., 2010. Anisotropic dispersion and attenuation due to wave-induced fluid flow: quasi-static finite element modeling in poroelastic solids, *J. geophys. Res.,* **115,** B07204, doi:10.1029/2009JB006644.

Zhu, Y. & Tsvankin, I., 2006. Plane-wave propagation in attenuative transversely isotropic media, *Geophysics,* **71**(2), T17–T30.

Zhu, Y., Tsvankin, I., Dewangan, P. & van Wijk, K., 2007. Physical modeling and analysis of *P*-wave attenuation anisotropy in transversely isotropic media, *Geophysics,* **72**(1), D1–D7.